

# Isolator-Less Near-Field RFID Reader for Sub-Cranial Powering/Data Link of Millimeter-Sized Implants

Christopher Sutardja<sup>✉</sup>, Member, IEEE, and Jan M. Rabaey, Fellow, IEEE

**Abstract**—Implants for brain-machine interface (BMI) systems require both wireless powering and data communication to be practical for reliable long-term use. Sub-cranial radio-frequency identification (RFID) readers can receive backscattered data, while providing wireless power to operate the implant. This paper presents a novel reader architecture for an efficient near-field fully integrated RFID reader meant to deliver power to and receive data from BMI implants, where a modified Class-E/Fodd power amplifier (PA) with a current-sense resistor differentially drives a single segmented antenna and acts simultaneously as TX and RX. It operates at 309 MHz and has 54% efficiency. The non-linearity of the switching PA is able to demodulate the backscattered signal to baseband. And the data can be recovered from a current-sense resistor without the need for bulky RF isolators, separate RX/TX antennas, or different frequencies for data/power delivery. The reader, as tested with a proprietary RFID tag through pig-skin and cow-bone, can deliver a maximum of 790  $\mu$ W to an implant through the skull while consuming 39.4 mW of power. It has a 2-Mb/s data rate with a bit error rate of less than 1e-6.

**Index Terms**—Brain, low power, near-field powering, power amplifier (PA), radio-frequency identification (RFID) reader, switching power amplifier (PA).

## I. INTRODUCTION

INTERFACING electronics with the human body has huge potential to improve healthcare and science. Specifically, brain-machine interfaces (BMIs) have the ability to revolutionize neuroscience while enabling new types of prosthetics driven by neural signals. Implants with the ability to acquire neural signals are crucial to these technologies. Neural implants have been getting more efficient and less invasive. A 1 mm<sup>3</sup> remotely powered transponder meant for neural implants was demonstrated in [1], and a 64-channel wireless electrocorticography (ECoG) implant was presented in [2]. Most attention has been given to the implant side of these BMI systems. A practical implementation of a long-term wireless neural recording system for BMIs [3] requires a compact and efficient external radio-frequency identification (RFID) reader

Manuscript received November 25, 2017; revised February 22, 2018; accepted March 19, 2018. Date of publication May 8, 2018; date of current version June 25, 2018. This paper was approved by Guest Editor Andrea Bevilacqua. This work was supported by the Sponsors of BWRC, TSMC, and DARPA. (*Corresponding author: Christopher Sutardja.*)

The authors are with the Department of Electrical Engineering and Computer Science, University of California, Berkeley, CA 94720 USA (e-mail: chris\_sutardja@berkeley.edu).

Color versions of one or more of the figures in this paper are available online at <http://ieeexplore.ieee.org>.

Digital Object Identifier 10.1109/JSSC.2018.2822673

to deliver power to and receive backscattered data from BMI implants. It is attractive to deliver power to and communicate with these implants wirelessly in order to lower the risk of infection and to limit the number of surgeries needed to replace batteries. This external reader must be able to safely deliver power to the implant, while robustly receiving data from it. To create a practical BMI system, it has to be something that people are willing to wear on top of their heads.

Communication using RFID backscattering is well suited for a data link through the skull. The external reader on top of the head provides a carrier to the tag underneath the skull, and the tag passively modulates its own impedance to communicate with the reader. However, backscattering systems suffer from TX-to-RX carrier leakage that may saturate receiver front-ends, and excess phase noise from the TX that can lower receiver sensitivity. Implanted tags with separate coils for powering and data telemetry like [4] and [5] take up too much space inside the skull. Some systems [4], [5] have the tag multiply the carrier frequency before backscattering, but that results in increased implant complexity, and a link that is difficult to optimize for both powering and data communications. For single coil links, off-chip components such as circulators and isolators can isolate RX from TX, but are too bulky. Also, the isolation of the circulators is limited by return loss of the matching network [6]. Fig. 1 illustrates the flaws of conventional isolation methods for RFID. Also, the systems in [4], [5], and [7] deliver wireless power to implants using carriers ranging from 13.56 to 25 MHz. Although loss through tissue is low at these frequencies, these frequencies of operation require the coil sizes of the implant to be larger than millimeter (mm)-scale to maintain a high Q.

This paper proposes a compact, single antenna RFID reader with a novel ammeter-based data-recovery method to reject the interferer from an efficient TX using a Class-E/Fodd switching power amplifier (PA) operating at 309-MHz carrier frequency. The rest of this paper is organized as follows. In Section II, we give an overview of the challenges in designing compact RFID readers meant to act as a powering/ data link for sub-cranial implants. Section III details the design of the IC. Section IV describes the safety concerns and the optimization of the reader's antenna to maximize efficient power delivery to the implant. Electronic and *in vitro* measurement results are described in Section V. And finally, the conclusion will be given in Section VI.

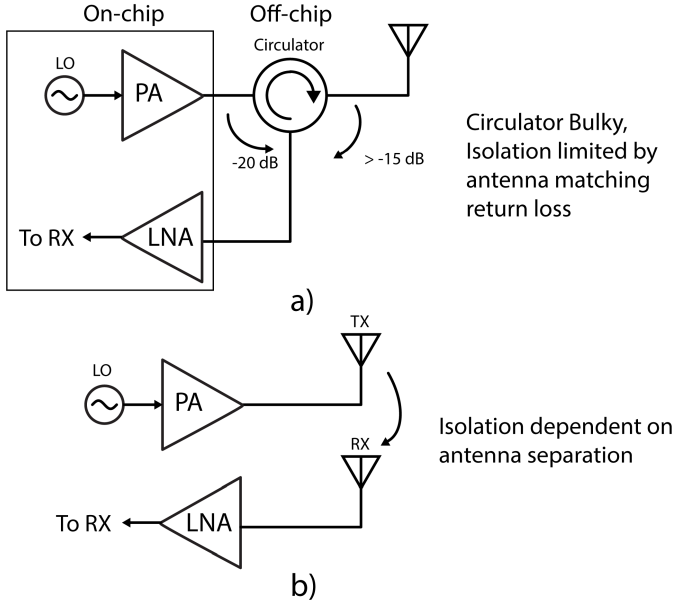


Fig. 1. Limitations of conventional RFID architectures using (a) off-chip circulator to isolate transmit from receive and (b) separate antennas for transmit and receive.

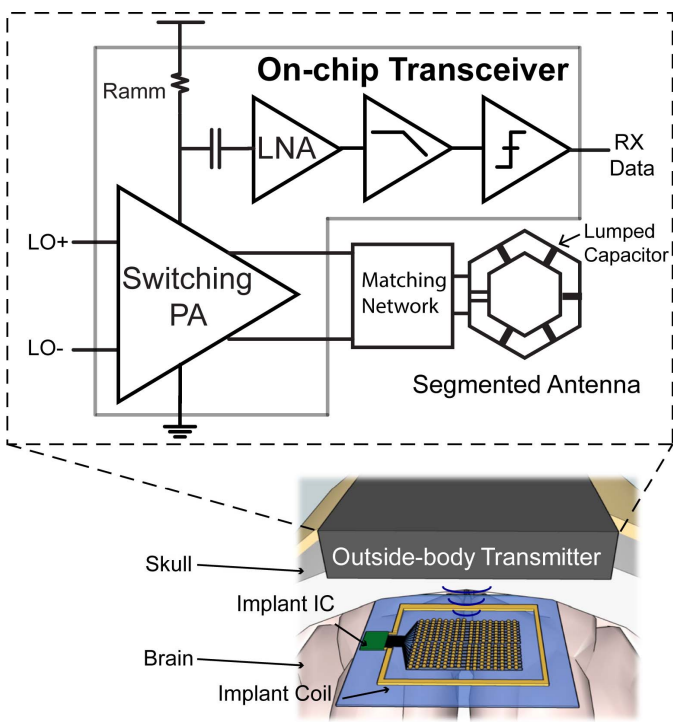


Fig. 2. Transcranial link diagram and transceiver architecture.

## II. SYSTEM-LEVEL DESIGN

### A. System Architecture

Fig. 2 shows the system diagram of the proposed RFID reader. The transceiver is intended to deliver power to and receive data from the implant in [2]. The transmitter consists of a Class-E/Fodd PA [8] driving a segmented loop antenna at 309 MHz. The receiver uses a novel method of interference rejection, as illustrated in Figs. 3 and 4. An ammeter resistor measures the current drawn from the power supply of the PA.

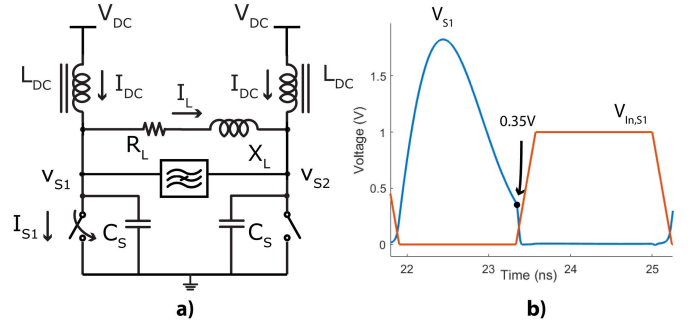


Fig. 3. (a) High-level schematic and operation of Class-E/Fodd PA. (b) Simulated switch drain waveforms.

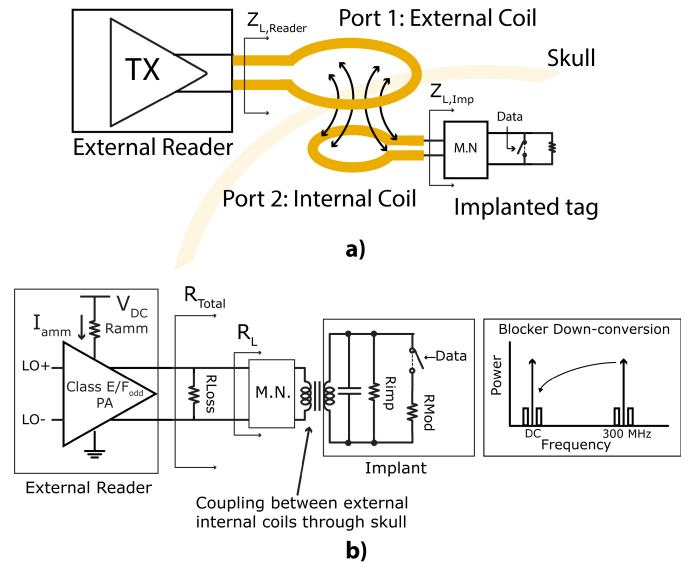


Fig. 4. (a) Two-port model of transcranial link. (b) Backscatter demodulation mechanism.

Because the reader and the tag are near-field coupled, the tag's impedance modulation will affect the load impedance seen by the PA of the reader, and hence the dc current drawn from the supply by the PA, which depends directly on its load. The non-linearity of the switching PA effectively mixes the backscatter of the tag down to dc, and spectrally separates the desired backscatter signal from the PA's output without the need for any external circulator or isolator. Any leakage current at RF can be filtered with simple low-pass filters built into the baseband amplifier chain (see Fig. 2), while any dc offset is filtered with a dc blocking capacitor. The data are encoded using Miller modulation, moving information away from dc, so the dc blocking capacitor does not introduce any loss to the desired signal.

### B. Class-E/Fodd Power Amplifier

The Class-E/Fodd PA, shown in Fig. 3, is a non-linear switching PA topology that was first introduced in [8]. It uses differential switches to drive a tuned differential load. Because the load is differentially driven, current at even harmonics does not flow through it. In addition, there is a parallel LC tank tuned to the fundamental frequency connected in parallel to the load to ensure that all higher order harmonics

are differentially shorted. The purpose of a tuned switching PA is to deliver power to a load at high efficiency. One of the primary mechanisms of loss in a switching PA is through the drain capacitance of the switches. As seen from Fig. 3, every cycle, there is a  $CV^2$  loss through each switch in the PA. Tuned switching PAs shape the waveform on the drain of the PA to resemble a half sinusoid so that when the switches turn ON, the voltage across the switch is close to zero.

### C. Blocker Rejection Method

The Class-E/Fodd PA has an interesting property where the dc current that the PA draws from the supply is dependent on only two parameters, the load resistance and the voltage of the power supply. According to [8], for a Class-E/Fodd PA

$$I_{dc} = \frac{\pi^2 V_{dc}}{4R_L}. \quad (1)$$

Fig. 4 shows that the load impedance connected to the implant coil is weakly near-field coupled to the external reader's segmented antenna. As a result, any change to the load impedance of the implant changes the load impedance seen by the PA. If a series resistor is inserted in series between the power supply and the Class-E/Fodd PA, then it can act as an ammeter that measures the change in current as the load impedance of the implant changes. The recovered baseband signal  $V_{Signal}$  across the ammeter resistor  $R_{amm}$  is given by

$$V_{Signal} = R_{amm} * \Delta I_{amm} \quad (2)$$

where  $\Delta I_{amm}$  ( $I_{amm} = 2I_{dc}$ ) depends on both the modulation depth of the implant tag and the coupling between the coils of the reader and implant.

Because the dc-feed inductor is not ideal, some leakage current at the TX carrier frequency will flow through the ammeter resistance, but the desired backscatter signal from the implant is already spectrally separated from the interference, so low-order baseband filters can filter out any interference.

### D. Effect of Link on Antenna Impedance

Considering that the external loop and internal loop are passive structures, the overall link parameters can be modeled through two-port Z-parameters [9]. The impedance looking into the external loop is given by

$$Z_{L,Reader} = Z_{11} - \frac{Z_{12}Z_{21}}{Z_{22} + Z_{L,Imp}}. \quad (3)$$

The desired recovered signal is based on the impedance  $\Delta Z_{L,Reader}$  when the implant's load impedance  $Z_{L,Imp}$  changes as follows:

$$\Delta Z_{L,Reader} = \frac{Z_{12}Z_{21}}{Z_{22} + Z_{L,Imp}} - \frac{Z_{12}Z_{21}}{Z_{22} + (Z_{L,Imp} - \Delta Z_{L,Imp})} \quad (4)$$

where port 1 refers to the terminals of the reader antenna and port 2 refers to the terminals of the implant antenna.

$\Delta Z_{L,Imp}$  is the change in the load impedance of the implant impedance during backscatter communications. The change in the real impedance of the reader antenna is then given by

$$\Delta R_{L,Reader} = \text{real}(\Delta Z_{L,Reader}) \quad (5)$$

which results in

$$\Delta I_{amm} = \frac{\pi^2 V_{dc}}{2(R_{L,reader} - \Delta R_{L,Reader})} - \frac{\pi^2 V_{dc}}{2R_{L,Reader}}. \quad (6)$$

### E. Effect of PA Efficiency on Backscatter Recovery

The calculations above assume 100% switching PA efficiency. In reality, switching PAs have significant loss that can affect the load impedance seen by the reader. For a lossy TX PA, the change in ammeter current is given by

$$\Delta I_{amm} = \frac{\pi^2 V_{dc}}{2(R_{Total} - \Delta R_{Total})} - \frac{\pi^2 V_{dc}}{2R_{Total}}. \quad (7)$$

Fig. 4 highlights the factors which determine the strength of the recovered signal  $\Delta I_{amm}$ . To maximize the detected signal  $\Delta I_{amm}$  by the ammeter, the change in the total impedance seen by the outputs of the PA  $\Delta R_{Total}$  must be maximized.  $R_{Total}$  can be approximated by the parallel combination of the load resistance of the antenna  $R_L$  and the equivalent parallel loss resistance  $R_{Loss}$ . As shown in (4), the antenna resistance  $R_L$  changes by  $\Delta R_L$  based on the modulation depth of the implant, the coupling factor between reader and implant coils, and the impedance of the implant. In a zero-voltage switching PA with relatively low switch on-resistance,  $R_{Loss}$  is dominated by the equivalent parallel resistance of the inductor  $L_{Tank}$  of the parallel LC tank of the Class-E/Fodd PA. Calculation of  $\Delta R_{Total}$  is as follows:

$$\Delta R_{Total} = \frac{(R_L + \Delta R_L)R_{Loss}}{(R_L + \Delta R_L) + R_{Loss}} - \frac{R_L R_{Loss}}{R_L + R_{Loss}} \quad (8)$$

$$\Delta R_{Total} \approx \frac{\Delta R_L R_{Loss}}{R_L + R_{Loss}}. \quad (9)$$

This result shows that making the equivalent parallel resistance  $R_{Loss}$  as large as possible maximizes the detected signal on the ammeter. The method of achieving this high  $R_{Loss}$  would be to maximize the Q of LC-tank inductor  $L_{Par}$ .

### F. Target System: 64-Channel uECOG Neural Implant

An RFID reader meant for sub-cranial powering and communications should be designed to power and communicate with an actual neural implant. A minimally invasive 64-channel wireless ECoG implant was designed by a colleague in [2]. The device consists of a highly flexible polymer-based 64-channel electrode array and a flexible antenna, bonded to a CMOS integrated circuit that performs 64-channel signal acquisition from the surface of the cerebral cortex and wireless data transmission. The implant also derives its supply from external wireless power transfer. It requires 225  $\mu$ W of power and transmits data at 1 Mb/s. The system requirements are specified in Table I. The external RFID reader was designed to surpass the maximum power delivery and received data rate requirements of the ECoG implant.

TABLE I  
UECOG IMPLANT PARAMETERS

Recording Modality	Electrocorticography (ECoG)
Channel Bandwidth	1-500 Hz
Number of Channels	64 Simultaneous
Uplink Data Rate	1 Mb/s
Required Power at Antenna	225 $\mu$ W
Carrier Frequency	$\sim$ 300 MHz
Implanted Antenna Diameter	6.5 mm

### III. INTEGRATED CIRCUIT

The integrated circuit consists of both transmit and receive circuitry. The transmitter consists of a Class-E/Fodd PA that is driven by a buffer chain. The receiver consists of a single-ended baseband LNA and subsequent baseband amplification and filtering stages. Having a high-efficiency PA also improves the signal strength of the recovered backscatter signal. As shown in (9), if most of the PA power consumption is delivered to the load antenna instead being burned in the PA, then the change in the PA's load impedance by backscattering will result in a larger change in the current drawn from the supply.

#### A. Transmitter Design

The TX PA is designed using a modified Class-E/Fodd topology. The two separate large dc-feed inductors and the inductor of the parallel *LC* tank are replaced by a single symmetric inductor that has a center tap connected to the supply. This modified design saves area on the chip while allowing a higher *Q* inductor to be used for both the *LC* tank and the dc-feed inductors.

1) *Symmetric Inductor*: In addition to having a high enough *Q* to minimize losses through the *LC* tank, the equivalent parallel resistance of this inductor must be sufficiently large compared to the load impedance of the PA, so that the majority of the current from the PA flows into its load. As a result, the inductor was designed to have as large of a *Q* as possible given the area constraints of the chip. To increase the inductance, the symmetric inductor was designed to have nine turns. Even with nine turns, the self-resonant frequency of the inductor is still 1.2 GHz, far higher than 300-MHz operating frequency of the PA.

2) *PA Impedance at Harmonics*: Class-E/Fodd operation requires there to be high impedance from the output nodes of the PA to the power supply [8]. Fig. 5 shows that the voltage at the drains of Class-E/Fodd PAs has both differential and common-mode components. To ensure that the PA remains in Class-E/Fodd operation, the impedance seen from output to supply must be large compared to the load being driven. Using separate dc choke inductors for each side of the PA accomplishes the goal of high impedance at both common-mode and differential-mode components of the PA output to the dc supply. However, this TX design combines the parallel *LC*-tank inductor and the two dc-feed inductors of a classic Class-E/Fodd PA into one large center-tapped symmetric

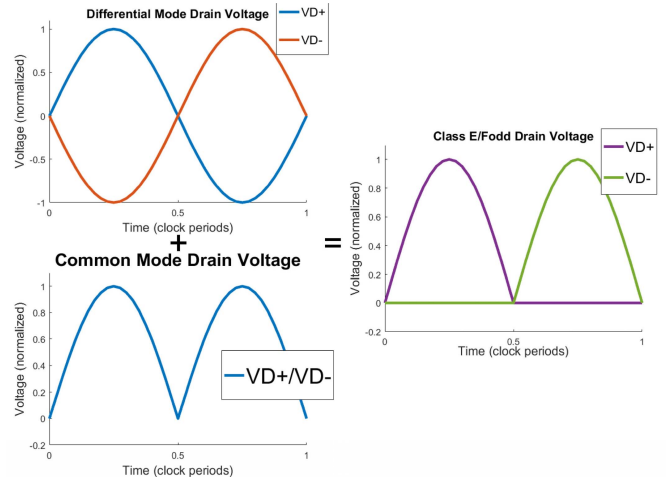


Fig. 5. Differential and common-mode components of Class-E/Fodd waveforms.

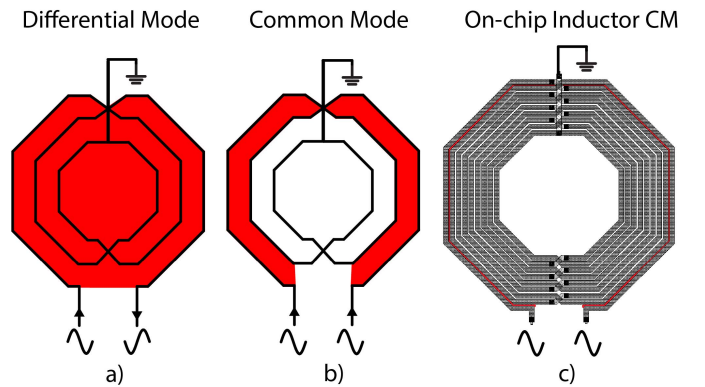


Fig. 6. Magnetic field, shown in red, generated by (a) three-turn symmetric inductor operating in differential mode, (b) three-turn symmetric inductor operating in common mode, and (c) on-chip nine-turn symmetric inductor operating in common mode.

inductor to save area and reduce the number of external components.

Even though the symmetric inductor has a high differential inductance, the common-mode inductance is low because there are nine turns that are closely wound together [10]. The path from the positive terminal of the inductor to the center tap is wound in the opposite direction as the path from the negative terminal of the inductor to the center tap. Fig. 6 illustrates the difference in magnetic field induced in between common-mode and differential operation of a center-tapped symmetric inductor. In common-mode operation, this results in most of the flux generated by one side of the inductor to be almost equal in magnitude but opposite in direction to the flux generated by the other side of the inductor, creating a low inductance path of less than 1 nH from the common mode of the PA to the supply. This low inductance causes there to be especially small impedance from the output to the supply at the 2nd harmonic.

To solve this issue, an extra inductor  $L_{dc}$  is put in between the center tap of the inductor to increase the common-mode inductance without changing the differential inductance of the PA. Without capacitors added in parallel, the common-mode impedance of the inductor tap to the supply at even

### On-Chip TX Switching PA

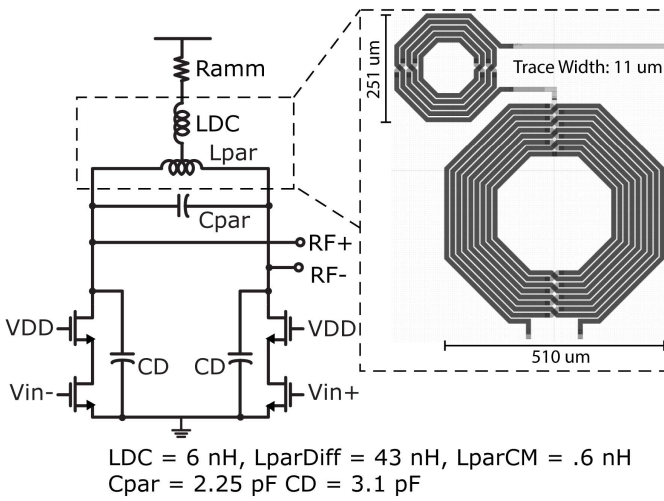


Fig. 7. Final design of on-chip TX PA.

harmonics is

$$X_{dc} = \omega(L_{Par,CM} + L_{dc}). \quad (10)$$

To increase the impedance seen by the common mode at the 2nd harmonic, extra capacitance  $C_{dc}$  is added in parallel with the output switches of the PA to resonate with this increased common inductance at the 2nd harmonic of the transmitted carrier. The final design for the modified Class-E/Fodd is shown in Fig. 7. The expression for the resonant frequencies  $\omega_{Diff}$  for the differential load of the PA is

$$\omega_{Diff} = \frac{1}{\sqrt{L_{par,Diff} * (C_{par} + C_{dc} + C_{D,switch})}}. \quad (11)$$

And the expression for the 2nd harmonic resonant frequency  $\omega_{CM}$  for the common-mode impedance of the PA is

$$\omega_{CM} = \frac{1}{\sqrt{(L_{par,CM} + L_{dc}) * (C_{dc} + C_{D,switch})}}. \quad (12)$$

*3) Switch Design:* The differential switches of the PA were designed with a cascode topology to increase the maximum voltage allowed at each output node of the PA before device breakdown. The primary causes of loss for PA switches are the  $CV_{DD}^2$  loss of the stages driving the PA output stage and the loss from the finite series resistance of the switches themselves. The transistors were sized to balance both sources of loss.

### B. Receiver Design

To recover the backscattered signal from the implant, the receive chain is connected to 1- $\Omega$  ammeter resistor that is connected in series with the power supply of the transmitter. The received signal from the implant is Miller encoded to ensure that there is no frequency content at dc. This encoding allows the receiver of the reader to filter out any dc offset from the backscattered signal using 30-pF series blocking capacitor.

### RX Baseband Amplifiers and Low-pass Filters

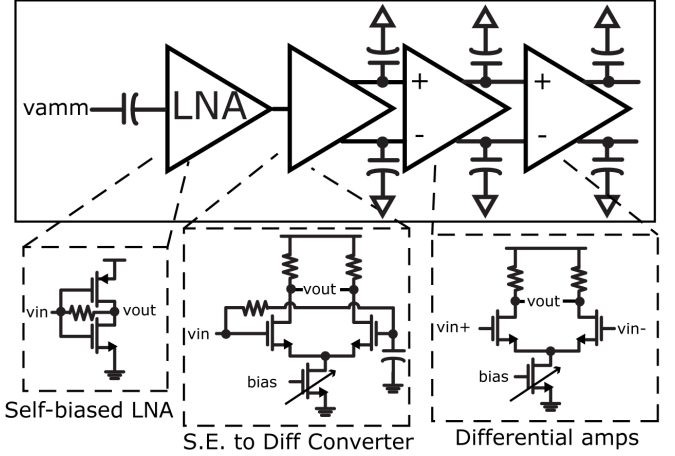


Fig. 8. RX baseband implemention.

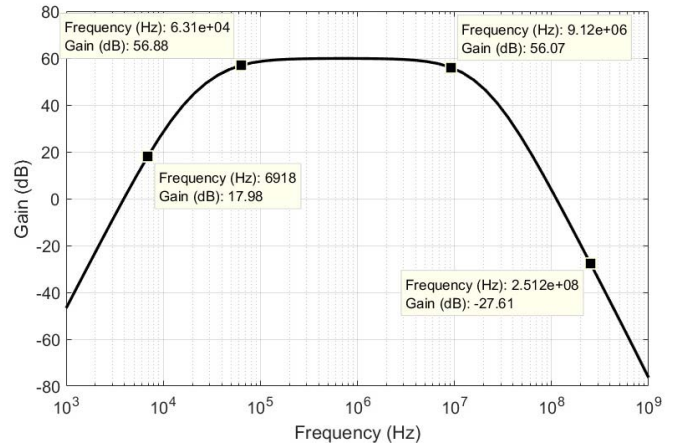


Fig. 9. RX baseband transfer function.

*1) Baseband Amplification and Filtering:* The baseband amplification stages are shown in Fig. 8. The LNA is followed by a differential pair acting as a single ended to differential converter and amplifier. This stage drives two subsequent stages of differential pairs to create a total gain of 60 dB for the receive chain of the reader.

Although the desired signal has already been demodulated down to baseband, there is still some leakage at RF due to the finite Q of the PA inductors. Each amplifier stage, including the LNA, has extra capacitance added to the output to act as a first-order low-pass filter. In total, there are four such amplifier stages, creating 4th-order low-pass filter that can heavily attenuate any interference from the carrier. Using capacitors of less than 10 pF, a blocker rejection ratio of  $-75$  dB is achieved at the output of the amplifier chain. Fig. 9 shows the transfer function of the RX amplifier chain. At the frequencies of the backscattered signal, the amplifier chain has about 60 dB of gain, while at the frequency of the TX leakage at RF, there is a gain of  $-15$  dB. As shown in Fig. 10, this blocker rejection of  $-75$  dB, combined with the push-pull topology of the LNA, is able to ensure that there is only 1.5 dB of gain compression at a carrier leakage magnitude

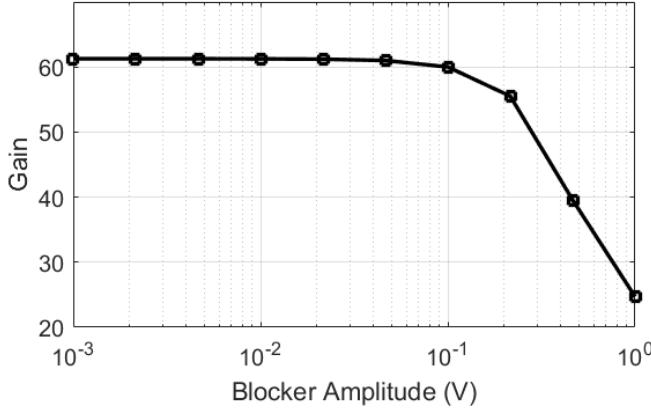


Fig. 10. Simulated gain versus blocker amplitude of receiver chain.

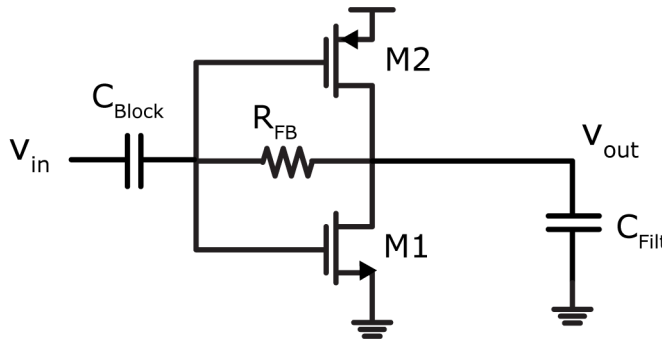


Fig. 11. LNA schematic.

of 100 mV. The typical simulated blocker amplitude at the ammeter is at 10 mV.

2) *Modulation and DC Offset Cancellation:* The ECoG implant uses Miller encoding to communicate with the reader in order to make it easier to filter the interfering carrier away from the received backscatter. Miller encoding is a way to code data so that a transition always happens every 2–4 cycles depending on the data pattern being generated. These frequent transitions ensure that there is very little information at dc.

Because the ammeter-based RFID reader directly down-converts the received signal to be centered at dc, any interference present from the carrier will also be down-converted to dc. Encoding the data using Miller modulation ensures that a simple first-order high-pass filter can be used to cancel out any dc offset.

3) *LNA Design and Receiver Sensitivity:* There are several requirements of the first-stage amplifier of the receive chain. The LNA should consume a small fraction of the power of the transmitter while maintaining high enough sensitivity to recover the backscattered signal. The amplifier should be linear enough to make sure that any local oscillator (LO) leakage from the transmitted carrier does not saturate the amplifier. And the input impedance should be high enough so that the corner frequency of the high-pass filter created by the dc blocking capacitor and the input impedance of the amplifier are lower than the lowest frequency content of the Miller-modulated data required. The self-biased inverter-based amplifier shown in Fig. 11 satisfies all three requirements.

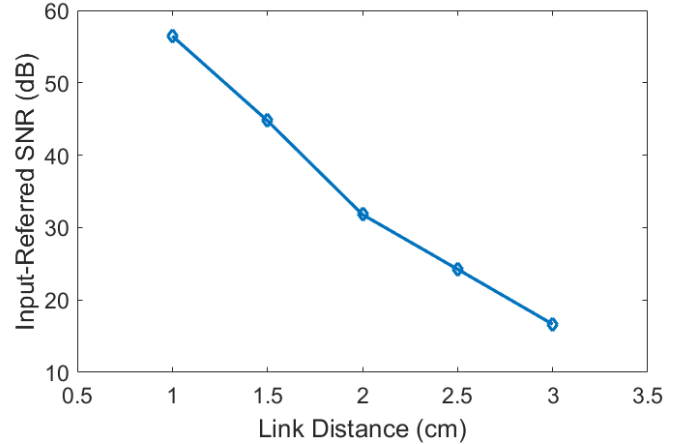


Fig. 12. Simulated input-referred SNR versus link distance of the receiver.

The gate and drain are connected by a large bias resistor, ensuring that the dc bias of the input and output of the amplifier keeps both PMOS and NMOS devices biased in saturation. The design is efficient because the complimentary input devices give two sources of  $g_m$  for only one bias current. The total  $g_m$  of the LNA is  $g_{m1} + g_{m2}$ , so the input-referred noise power spectral density would be

$$v_{n,\text{input}}^2 = \frac{4kT}{g_{m1} + g_{m2}} \frac{\gamma}{\alpha} \Delta f. \quad (13)$$

The main contribution to amplitude noise would be the first-stage LNA. And the total input-referred noise voltage at the frequency band of the LNA would be approximately

$$v_{n,\text{integrated}}^2 = \int \frac{4kT}{g_{m1} + g_{m2}} \frac{\gamma}{\alpha} |H_{\text{LNA}}(f)|^2 df \quad (14)$$

where

$$H_{\text{LNA}} = \frac{2\pi f * R_{\text{in}} C_{\text{Block}}}{1 + 2\pi f R_{\text{in}} C_{\text{Block}}} \frac{1}{1 + 2\pi f * R_{\text{out}} C_{\text{filt}}}. \quad (15)$$

Also, these complimentary input transistors are also more tolerant of higher swings. The simulated amplitude of the backscatter signal on the ammeter is simulated to be 173  $\mu$ V at link distance of 1.5 cm, so the ammeter was sized to have an input-referred integrated noise voltage with a 1- $\mu$ V standard deviation to ensure robust low bit error rate (BER) in the receiver. The input-referred SNR versus link distance is shown in Fig. 12.

### C. Phase Noise Rejection

For RFID readers, phase noise leakage from the LO of the TX to the RX is often the primary cause of lowered receiver sensitivity [11]. As seen from Fig. 13, the switching operation of the Class-E/Fodd PA clips any amplitude noise from the input clock to the PA. Mixing down the carrier of the received signal with a carrier with correlated phase noise lowers the contribution of the phase noise [12]. In this ammeter-based PA transceiver, the same clock simultaneously generates the carrier for the received backscatter, while demodulating the received backscatter back to dc, so sensitivity is primarily limited to the LNA performance.

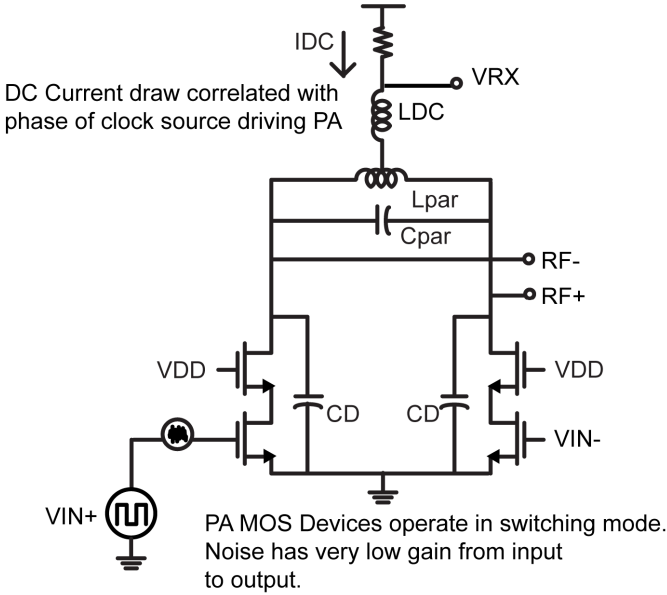


Fig. 13. Transceiver phase noise rejection.

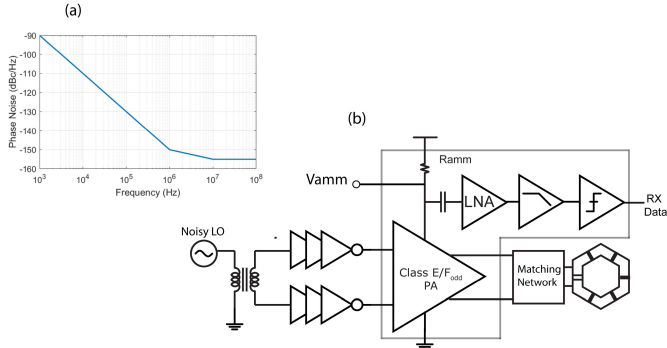


Fig. 14. (a) Phase noise spectrum of LO and (b) simulation model used to determine effect of down-converted phase noise on receiver sensitivity.

Although the ammeter-based reader down-converts the desired backscatter signal to baseband, it also down-converts the phase noise of its own LO to baseband. Variations in the phase of the input signals driving the differential switches of the Class-E/Fodd PA could potentially change the current through the  $R_{\text{amm}}$ . The voltage induced on the  $R_{\text{amm}}$  by the integrated down-converted phase noise power can lower the sensitivity of the receiver. Fig. 14 shows the setup of the phase noise experiment. The effect of phase noise was simulated by using a sine wave with a similar phase noise power spectral density to a typical RF signal generator. This sine wave is passed through a single ended to differential converter and fed into a chain of inverters to limit its amplitude to that of a square wave. Then, the effect of the phase noise on  $V_{\text{amm}}$  was measured through harmonic balance simulation.

To calculate the effective dBc/Hz of the phase noise signal, the dc current through the ammeter needs to be compared to the noise spectral density of the current of the down-converted phase noise at  $V_{\text{amm}}$ . The difference in decibel between the down-converted phase noise current and the dc current through the ammeter  $R_{\text{amm}}$  is the relative phase noise spectral density in dBc/Hz. Fig. 15 shows the phase noise density.

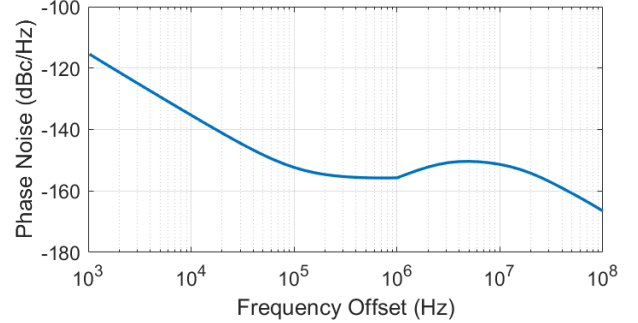
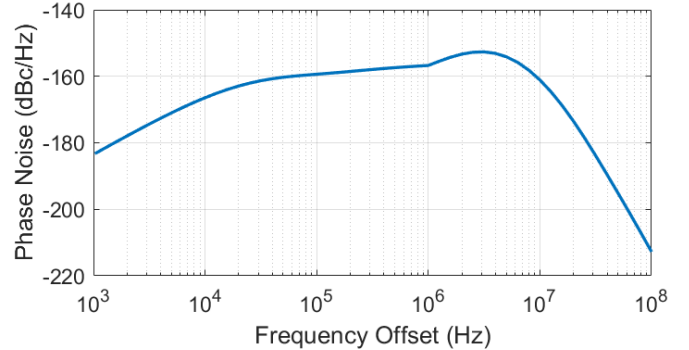
Fig. 15. Phase noise versus frequency offset at  $V_{\text{amm}}$ .

Fig. 16. Phase noise versus frequency offset input referred to receiver input.

The high-pass characteristic of the baseband receive chain is helpful in reducing the impact of the baseband down-converted phase noise. Fig. 16 shows the input-referred phase noise versus frequency spectrum in dBc/Hz at the ammeter input when the baseband transfer function from Fig. 9 is applied.

The integrated noise voltage over this bandwidth is less than 600 nV, significantly lower than the designed LNA input-referred noise of 1  $\mu$ V. This is another advantage of using Miller encoding. As shown in Fig. 15, a large portion of the phase noise is situated close to the carrier. Using Miller encoding moves frequency content of the backscatter signal away from the carrier, so the phase noise that is close to the carrier can be filtered out with simple high-pass filters.

#### IV. POWER DELIVERY

##### A. Antenna Design

The primary limitation for wireless power transfer in the human body is specific absorption rate (SAR). SAR is defined as

$$\text{SAR} = \frac{\sigma |E|^2}{\rho} \quad (16)$$

where  $E$  is the electric field,  $\sigma$  is the conductivity of human tissue, and  $\rho$  is the mass density of the human tissue. Even though a loop antenna with a 1.6-cm diameter is small compared to the wavelength of a 300-MHz carrier in human tissue, its length is still electrically significant enough to induce a nonuniform electric field in the human tissue below it. These electric field hotspots can limit the maximum power able to be delivered from the reader to the implant through the skull.

To solve this problem, a hexagonal loop antenna that is segmented by series capacitors was designed [13]. These series capacitors resonate out the inductance of the antenna and spread the electric field evenly throughout the tissue underneath the reader. This topology allows up to 30% more power to be delivered to the antenna while still satisfying the maximum SAR limit mandated by the FCC.

### B. Antenna Optimization

The antenna impedance is mostly inductive, and its dimensions are too small compared to the wavelength of the carrier to any significant radiation resistance. Therefore, to maximize the amount of power delivered by the antenna, the real part of the resistance of the antenna must be minimized. The segmenting capacitors do spread the electric field, but these surface mount components add a large amount of resistance in series with the coil. Even surface mount capacitors marketed as high-performance RF capacitors still have an ESR on the order of  $0.1 \Omega$  each. The five series segmenting capacitors can add  $0.5 \Omega$  to the antenna. To lower the loss from these series capacitors, instead of using one capacitor for each segment, the antenna was designed to have two capacitors in parallel to connect each segment of the loop with the next segment.

### C. Matching Network

The goal of the matching network is to maximize the efficiency of the transmitter while ensuring proper Class-E/Fodd operation of the transmit PA. The magnetic field generated by the transmit coil is dependent on the current through it. The impedance of the unmatched antenna is

$$Z_{\text{ant}} = \omega L_{\text{Ant}} - \frac{5}{\omega C_{\text{Seg}}} + R_{\text{Ant}} + R_{C_{\text{seg}}}. \quad (17)$$

With a parallel match, the impedance at the resonant frequency becomes

$$Z_{\text{match}} = (1 + Q_{\text{Ant}}^2) = R_{\text{Ant}} \quad (18)$$

where

$$Q_{\text{Ant}} = \frac{\omega L_{\text{Ant}} - \frac{1}{\omega C_{\text{Seg}}}}{(R_{\text{Ant}} + R_{C_{\text{seg}}})}. \quad (19)$$

Matching the antenna to a higher impedance lowers the effect of any series resistance from the printed circuit board (PCB) traces and bond-wires in between the antenna and the TX PA. Fig. 17 shows the design and dimensions of the segmented antenna and matching network and the simulated matched impedance of the antenna as a function of frequency.

The real part of the unmatched antenna impedance  $R_{\text{Ant}} + R_{C_{\text{seg}}}$  is both low and unpredictable because it comes primarily from the PCB trace impedance, the series resistance from the surface mount segmenting capacitors, and solder bumps used to attach the segmenting capacitors. As a result,  $Q_{\text{Ant}}$  and  $Z_{\text{match}}$  from (18) are difficult to predict exactly. This effect results in a matching network where the antenna is matched over a narrow band, and exact value of the impedance match is unpredictable. Fig. 17 shows the difference between measured and simulated real impedance of the matched

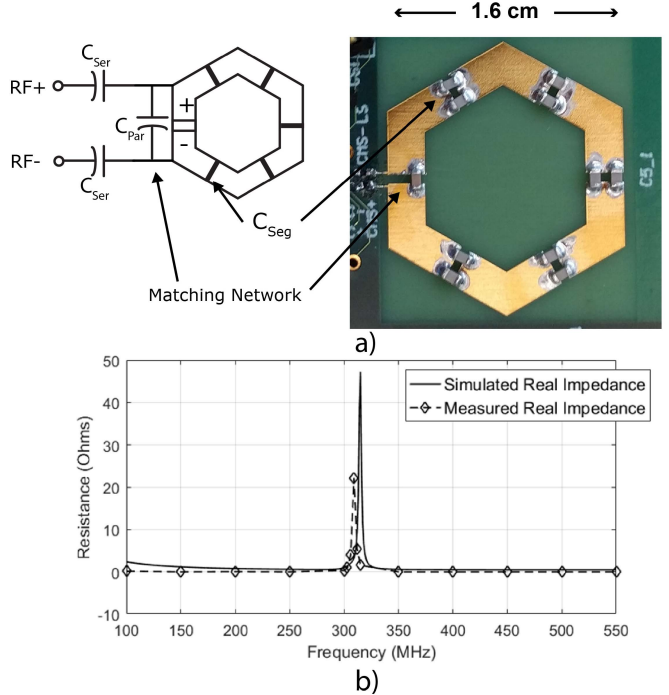


Fig. 17. (a) Segmented antenna and matching network. (b) Real part of simulated and measured matched antenna impedance.

antenna. Outside the center frequency of the matching network, the segmented antenna has a low impedance. With low load impedances ( $< 1 \Omega$ ) presented at its output, the Class-E/Fodd PA does not function efficiently. To ensure acceptable PA efficiency over a wider bandwidth, series capacitors are added in between the antenna and PA increase the impedance seen by the PA.

## V. MEASUREMENT RESULTS

The design was fabricated in 65 nm in a general-purpose CMOS process with seven metal layers, two thick metal layers, and one top-level aluminum layer from TSMC. A chip micrograph is shown in Fig. 18. The chip consists of a Class-E/Fodd transmitter and a baseband receive chain. The passive components of the PA, the filtering and amplification stages of the receiver, and biasing circuitry are all integrated on the die. Table II summarizes the overall performance of the link. The total chip area including pads is  $1.5 \text{ mm} \times 1.2 \text{ mm}$ . The active area of all the circuitry is  $.89 \text{ mm}^2$ . The area and power consumption of the IC are dominated by the Class-E/Fodd PA, which consumes 35 mW and has two large integrated inductors.

Table III lists the power and area breakdowns by block. As shown in Fig. 19, the chip is bond-wire packaged on a test PCB containing the segmented antenna and various testing structures.

### A. Proprietary Implant Tag

The reader was designed to deliver power to and communicate with an existing implant described in [2]. The implant chip is complex and consists of an RF transmitter, RF-dc power conversion circuitry, and 64-channels of amplifiers meant for

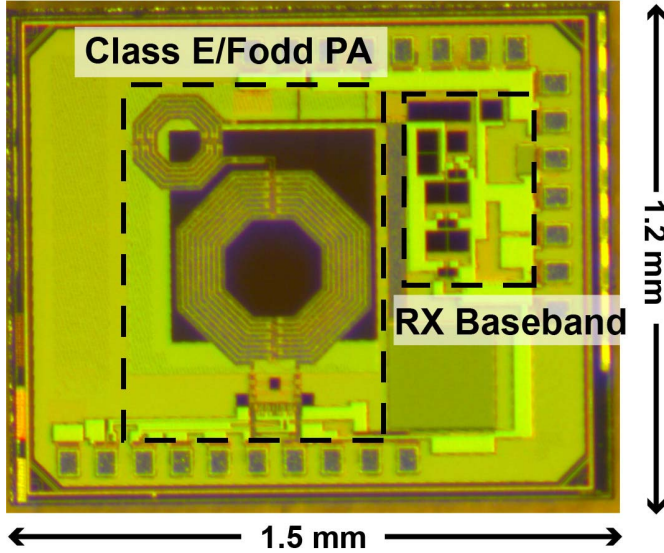


Fig. 18. Die photograph.

TABLE II  
SUMMARY OF SYSTEM PARAMETERS AND PERFORMANCE

System Parameter	This Work
External Antenna Diameter	1.5 cm
Internal Antenna Diameter	6.5 mm
Communication Distance	Transcranial 1 cm
Carrier Frequency	309 MHz
Data Encoding Scheme	Miller
Bit Error Rate	<1E-6
Transmit Power	35 mW
Received Power	790 $\mu$ W
Overall Link Efficiency	2.3 %

TABLE III  
MEASURED IC POWER AND AREA BREAKDOWN BY BLOCK

	Area	Power
TX Switching Amplifier	.66mm <sup>2</sup>	35 mW
RX Baseband Amplification	.23 mm <sup>2</sup>	4.4 mW
Total	.89 mm <sup>2</sup>	39.4 mW

neural signal acquisition. To simplify testing, a proxy board was designed to have the same antenna dimensions and similar impedance characteristics to the implant shown in Fig. 20. This board consists of a loop and surface mount components meant to replicate the load characteristics of the ECoG chip designed in [2]. A surface mount capacitor is placed in parallel with the loop antenna to act as a matching network. Parallel surface mount resistors with similar resistance values to the

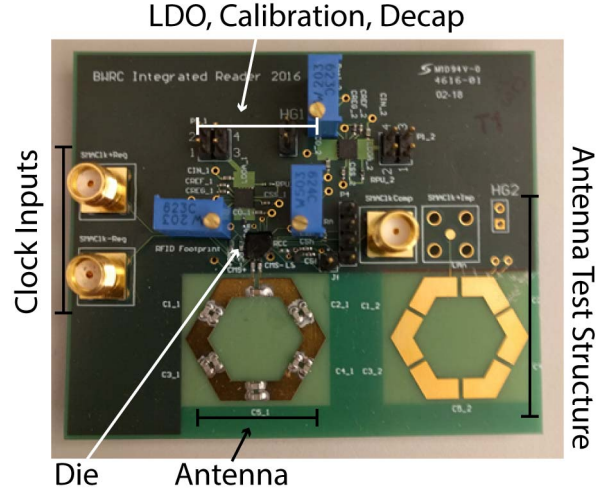


Fig. 19. Photograph of test PCB for reader.

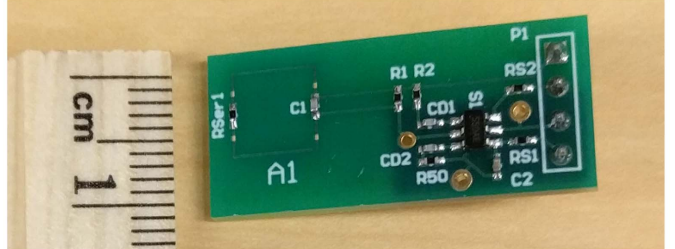
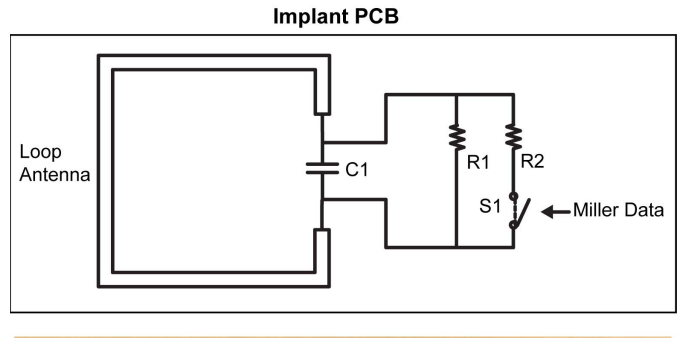


Fig. 20. Photograph and schematic of implant PCB.

rectifier in [2] are driven by the antenna. One of the resistors is connected in series with a switch so that the implant board can communicate through backscatter by modulating its load impedance. The switch is driven by an Opal Kelly field-programmable gate array board outputting a PRBS-7 Miller-encoded data pattern.

### B. Measurements in Air

Power transfer and data-link measurements were taken with the implant coil at various distances away in air to compare with existing transcranial data/power transfer systems in Table IV. At 1-cm coil separation, the design is able to deliver a maximum of 1.25 mW to the implant at a TX power consumption of 35 mW, for an overall link efficiency of 3.3%. Fig. 21 shows the BER versus link distance in air. The minimum BER is primarily limited by test equipment, specifically the amount of data the oscilloscope used can capture. Fig. 22 shows the overall link efficiency versus

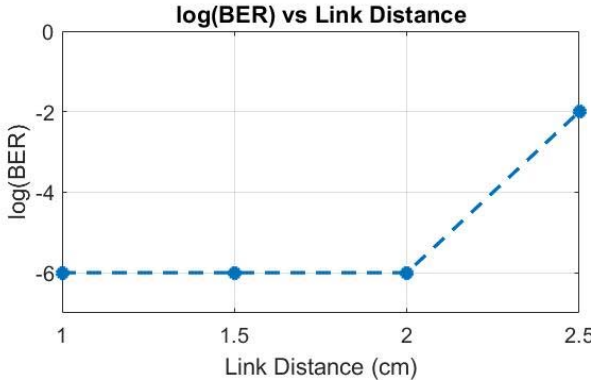


Fig. 21. BER versus link distance.

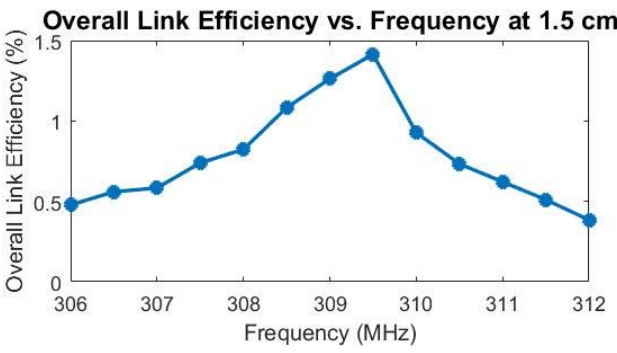


Fig. 22. Overall link efficiency versus frequency at 1.5-cm link distance.

TABLE IV  
COMPARISON WITH PRIOR ART

	2008 [7]	2012[4]	2015[5]	This Work
Powering Carrier (MHz)	25	5	13.56	<b>309</b>
Data Carrier (MHz)	25	46	50	<b>309</b>
Data Rate (Mb/s)	2.8	3	13	<b>2</b>
TX Coil Diameter (cm)	3.5	3	3.2	<b>1.6</b>
Implant Coil Diameter (mm)	35	10	10	<b>6.5</b>
Blocker Rejection Method	Envelope Detection	Different Data/Power Frequency	Different Data/Power Frequency	<b>Ammeter-Based</b>
Separate Power and Data coils?	No	Yes	Yes	<b>No</b>
BER	1E-06	2E-04	4.3E-07	<1E-06
TX Efficiency	N/A	N/A	61.8%	<b>54%</b>
Link Efficiency	N/A	N/A	19.3%	<b>3.3%</b>

frequency at a link distance of 1.5 cm. Overall link efficiency is found by taking the total amount of power delivered to the load of the implant and dividing that by the power consumption of the TX PA. This metric takes into account both PA efficiency and link loss. The link is measured at a distance of 1.5 cm in air since a channel that consists of a skull of thickness 1 cm will have a larger loss than a channel that is 1 cm in air. The PA's load is a highly tuned inductive load matched to a real

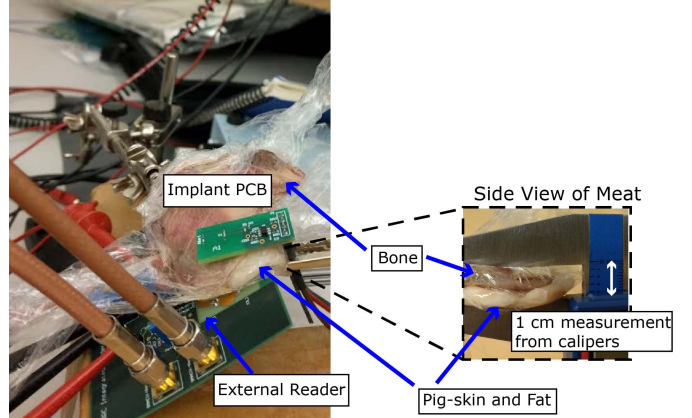


Fig. 23. Measurement setup with reader communicating with implant through proxy for human skull.

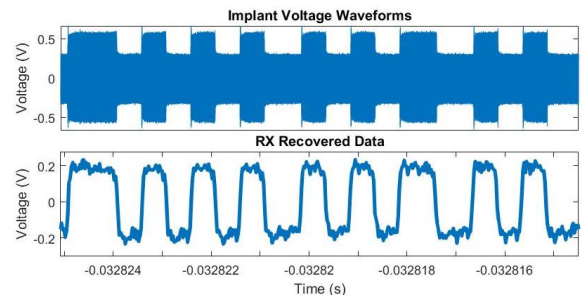


Fig. 24. Implant and RX waveforms.

impedance, so optimal power transfer occurs within a narrow band.

#### C. In Vitro Measurement

The RFID reader is designed to communicate through an adult human skull. Because of the difficulty in procuring a human skull, a channel meant to have similar loss characteristics to a human skull was constructed out of various meats from the grocery store. To create a medium similar to the skin and fat of a human scalp, we used the skin from a slab of pork belly with the fat layer significantly trimmed down. The flat part of the bone from a t-bone steak was used as a stand-in for the relatively flat geometry of the cranium bone from a human. The two pieces of meat were stacked on top of each other to create the channel shown in Fig. 23. The reader antenna was placed on the skin side of the channel, and the implant antenna was placed on the bone side of the channel. The design is able to deliver a maximum of  $790 \mu\text{W}$  to the implant at a TX power consumption of 35 mW, for an overall link efficiency of 2.3%. The power is primarily limited by the breakdown voltage of the cascode switches of the Class-E/Fodd PA. To prevent device breakdown, the peak-to-peak swing across the switches of the PA is limited to 2 V. The receiver's data rate with Miller modulation is 2 Mbps at a BER of less than  $1e-6$  with this configuration. Fig. 24 shows the backscatter waveforms from the implant and the recovered data from the reader's TX. The top graph measures the modulated carrier at the load of the implant, while the bottom graph shows the corresponding

down-converted at the output of the baseband receive chain of the RFID reader.

#### D. Comparison With State of the Art

Table IV summarizes the performance of the novel RFID reader compared to state-of-the-art transcranial links. Compared to other works, this reader uses a much higher frequency for power and data communications. This higher frequency allows both the TX coil and the implant coil to be much smaller. In addition, the ammeter-based architecture allows the external reader to be highly integrated for an even more compact form factor.

## VI. CONCLUSION

A novel blocker rejection method for a near-field RFID reader meant for sub-cranial links has been presented. The reader's ammeter-based receiver rejects blocker noise to create a sensitive receiver with low BER. The reader can receive Miller-modulated backscattered data at 2 Mb/s, and it can deliver up to 790  $\mu$ W of power to an mm-sized implant *in vitro*. The power and data links operate on the same carrier frequency of 309 MHz, which prevents the need for separate coils for data and powering. Also, implant design is simplified because no frequency generation circuitry is needed to generate separate carriers. Compared to other works, this work uses no external components to isolate TX from RX, and the TX Coil and implant coil have far smaller form factor.

This architecture can be applied over a wide range of frequencies for near-field power/data links in a wide variety of applications. As shown in (4) and (9), the performance of the transceiver improves as the strength of coupling between reader and implant increases and as efficiency of the switching PA increases. Improvements in either area would further push the performance limits of the system, allowing for efficient power delivery to many types of implants using wireless communications in the human body.

## ACKNOWLEDGMENT

The authors would like to thank TSMC University Shuttle Program for IC fabrication, Lorentz PeakView, Integrand EMX, and the students, staff, and faculty of the Berkeley Wireless Research Center.

## REFERENCES

- [1] M. Mark *et al.*, "A 1 mm<sup>3</sup> 2 Mbps 330 fJ/b transponder for implanted neural sensors," in *Symp. VLSI Circuits, Dig. Tech. Papers*, Honolulu, HI, USA, Jun. 2011, pp. 168–169.
- [2] R. Müller *et al.*, "A minimally invasive 64-channel wireless  $\mu$ ECG implant," *IEEE J. Solid-State Circuits*, vol. 50, no. 1, pp. 344–359, Jan. 2015.
- [3] F. Goodarzy, E. S. Skafidas, and S. Gambini, "Feasibility of energy-autonomous wireless microsensors for biomedical applications: Powering and communication," *IEEE Rev. Biomed. Eng.*, vol. 8, pp. 17–29, Aug. 2015.
- [4] S. Mandal and R. Sarapeshkar, "Power-efficient impedance-modulation wireless data links for biomedical implants," *IEEE Trans. Biomed. Circuits Syst.*, vol. 2, no. 4, pp. 301–315, Dec. 2008.

- [5] A. D. Rush and P. R. Troyk, "A power and data link for a wireless-implanted neural recording system," *IEEE Trans. Biomed. Eng.*, vol. 59, no. 11, pp. 3255–3262, Nov. 2012.
- [6] Y. D. Chen, "Reflective impulse radios: Principles and design," Ph.D. dissertation, Dept. Elect. Eng. Comput. Sci., Univ. California, Berkeley, CA, USA, 2013.
- [7] M. Kiani and M. Ghovanloo, "A 13.56-Mbps pulse delay modulation based transceiver for simultaneous near-field data and power transmission," *IEEE Trans. Biomed. Circuits Syst.*, vol. 9, no. 1, pp. 1–11, Feb. 2015.
- [8] S. Kee, "The class E/F family of harmonic-tuned switching power amplifiers," Ph.D. dissertation, Dept. Elect. Eng., California Inst. Technol., Pasadena, CA, USA, 2002.
- [9] S. J. Orfanidis. (2013). *Electromagnetic Waves and Antennas*. [Online]. Available: <http://eceweb1.rutgers.edu/~orfanidi/ewa/>
- [10] J. Chen, "Advanced architectures for efficient mm-Wave CMOS wireless transmitters," Ph.D. dissertation, Dept. Elect. Eng. Comput. Sci., Univ. California, Berkeley, CA, USA, 2014.
- [11] S. Chiu *et al.*, "A 900 MHz UHF RFID reader transceiver IC," *IEEE J. Solid-State Circuits*, vol. 42, no. 12, pp. 2822–2833, Dec. 2007.
- [12] E.-H. Kim, K. Lee, and J. Ko, "An isolator-less CMOS RF frontend for UHF mobile RFID reader," in *IEEE Int. Solid-State Circuits Conf. (ISSCC) Dig. Tech. Papers*, San Francisco, CA, USA, Feb. 2011, pp. 456–458.
- [13] T. Björninen, R. Müller, P. Ledochowitsch, L. Sydänheimo, L. Ukkonen, and J. Rabaey, "Antenna design for wireless electrocorticography," in *Proc. IEEE Int. Symp. Antennas Propag.*, Chicago, IL, USA, Jul. 2012, pp. 1–2.
- [14] H. M. Lee, M. Kiani, and M. Ghovanloo, "Advanced wireless power and data transmission techniques for implantable medical devices," in *Proc. IEEE Custom Integr. Circuits Conf. (CICC)*, San Jose, CA, USA, Sep. 2015, pp. 1–8.



**Christopher Sutardja** (S'09–M'18) received the B.S. and Ph.D. degrees in electrical engineering and computer sciences from the University of California at Berkeley, Berkeley, CA, USA, in 2010 and 2017, respectively.

His current research interests include low-power RF transceiver design, RF power amplifiers, and wireless power delivery.



**Jan M. Rabaey** (F'95) was the Faculty Member with the University of California at Berkeley, Berkeley, CA, USA, where he was a Research Manager at IMEC from 1985 to 1987, and also holds the Donald O. Pederson Distinguished Professorship. He is the Founding Director of the Berkeley Wireless Research Center, Berkeley, CA, USA, and the Berkeley Ubiquitous Swarm Lab, Berkeley, CA, USA, and has served as the Electrical Engineering Division Chair at Berkeley twice. He has made high-impact contributions to a number of fields, including

advanced wireless systems, low-power integrated circuits, mobile devices, sensor networks, and ubiquitous computing. His current research interests include the conception of the next-generation distributed systems, and the exploration of the interaction between the cyber and the biological world.

Prof. Rabaey is a member of the Royal Flemish Academy of Sciences and Arts of Belgium, and received honorary doctorates from Lund (Sweden), Antwerp (Belgium), and Tampere (Finland). He was a recipient of major awards, amongst which the IEEE Mac Van Valkenburg Award, the European Design Automation Association Lifetime Achievement Award, the Semiconductor Industry Association University Researcher Award, and the SRC Aristotle Award. He has been involved in a broad variety of start-up ventures, including Cortera Neurotechnologies, Berkeley, CA, USA, of which he is a Co-Founder.